Balloons over Volcanoes Scientific Report

Daniel C. Bowman, Patrick Gouge, Tierney Larson, Jacob F. Anderson, and Jonathan M. Lees

December 9, 2014

Contents

1 Introduction

Acoustic signals provide valuable information on natural and man made activity on the Earth's surface and the atmosphere. In addition, such signals can be used to infer atmospheric structure. The vast majority of acoustic studies utilize sensor networks on the surface of the Earth, despite the availability of the lower 50 km of atmosphere to balloon-mounted detectors. Such free flying arrays may offer distinct advantages, such as lack of wind noise, absence of anthropogenic signals, and elevation above the turbulent atmospheric boundary layer. They may also address important scientific questions such as the location and height of acoustic waveguides, the fraction of acoustic energy that contributes to ionospheric heating, and the possibility of novel signals that do not reach the Earth's surface. The Balloons over Volcanoes team proposed and launched a three element acoustic array into the stratosphere as part of the NASA High Altitude Student Platform (HASP) project to investigate the feasibility and scientific value of such free flying detectors.

    Our engineering objective was to demonstrate the operation of an airborne array in the extreme environment of near space. Our initial scientific objectives included correlation of acoustic signals between ground stations (see Figure 1) and the airborne array, investigating the intensity of waveguides at the tropopause,

searching for novel waveforms in the stratosphere, and evaluating wind noise intensity throughout the flight. The engineering objective was met, with successful operation of the acoustic array and data acquisition system throughout the flight. Two of the microphones also survived landing and continued to record data on the ground.

We detected a narrowband acoustic signal in the air and on the ground simultaneously as the balloon flew over an infrasound station south of Albuquerque, New Mexico, fulfilling our first scientific objective. Our proposal suggested searching for mine blasts on both ground stations and the balloon, but no blasts were recorded because the flight was on a Saturday. The presence of a waveguide at the tropopause could not be evaluated due to wind noise and rapid pressure changes during the ascent. The stratosphere had a number of unusual acoustic signals, most of which we did not recognize. Further investigation and experiments may reveal whether they are from known acoustic sources on the ground. We determined that wind noise is an impediment to acoustic recording in the lower 6,000 m of the atmosphere during ascent. Also, the rapid pressure drop caused two of our three microphones to "clip" (produce a higher voltage than our data logger could record) during ascent.

The most significant issues encountered during the experiment were microphone clipping during ascent and descent as well as deviation from the linear amplitude range of the detectors. While the latter decreases the reliability of absolute acoustic amplitude measurements, there is no reason to think the frequency content of the signals was adversely affected. Despite these problems, we consider the flight a near complete success, as we were able to satisfy our engineering objective and address most of our scientific questions.

2   Acoustic Array and Flight Characteristics

The flight hardware included a 11.82 million cubic foot zero pressure helium balloon, a parachute for descent, and an instrumentation gondola. The acoustic array consisted of three InfraNMT differential pressure transducers arranged in a vertical line on the flight ladder between the gondola and the parachute. The microphones were enclosed in insulated lunch coolers wrapped in white tape to prevent overheating (Figure 2). The transducers were named TOP, MID, and BOT, with TOP closest to the parachute and BOT closest to the gondola (Figure 3). Each station was separated by 6.6 m for a total network aperture of 13.2 m.

We used an Omnirecs DataCube digitizer to record signals from the microphones. The sample rate was 400 Hz and gain was set at 64. The digitizer was located on the gondola, inside a payload box consisting of white tape, thermal insulation, and a Plexiglas cover. A set of lithium batteries on the gondola provided power to the digitizer, but the microphones each had independent 9 volt lithium batteries.

The balloon was launched on August 9th, 2014 at 13:25 GMT (7:25 local time) from Ft. Sumner, New Mexico. It reached neutral buoyancy 15:37 GMT and remained at an average altitude of 37500 meters above sea level for the next 5.7 hours. The flight was terminated at 21:17 GMT; the gondola landed northeast of Flagstaff, Arizona, at 22:03 GMT (Figures 4 and 5).

All three microphones recorded data throughout the flight (Figure 6), but MID was destroyed on impact. Stations TOP and BOT exceeded the voltage range of the digitizer during most of the ascent and almost all of the descent. Station MID was clipped during the initial descent but later came back into the input voltage range of the digitizer. Differential pressures were in the range of linear amplitude response for about a third of the float phase. Pressures were generally below the linear amplitude scaling cutoff for the ascent and first two thirds of float, whereas they were above linear amplitude range during the descent.

3   Microphone Theory of Operation

We used InfraNMT differential pressure transducers (Marcillo et al., 2012) to detect infrasound during the flight. These sensors consist of two chambers: one open to the atmosphere, another coupled to the atmosphere via a mechanical low pass filter (Figure 7). A piezoelectric pressure transducer produces a voltage when a diaphragm between the two chambers is deflected.

The mechanical low pass filter is the acoustic analogue of an RC circuit. The acoustic resistance of a cylindrical channel is derived from the expression for Poiseuille flow (Mutschlecner and Whitaker, 1997):

$$R = \frac{8\eta}{\pi r^4} l \tag{1}$$

where η is the shear viscosity of the fluid, r is the radius of the capillary tube, and l is the length of the capillary tube. The acoustic capacitance is defined as

$$C = \frac{V}{\gamma \bar{P}} \tag{2}$$

where V is the backing volume, γ is the adiabatic gas constant, and $\bar{P}$ is the average background pressure. In Earth's atmosphere, the value of γ varies between 1.403 in pure adiabatic and 1 in pure isothermal conditions; this is dependent on the frequency of pressure fluctuations, air conditions, and chamber geometry (Marcillo et al., 2012). The adiabatic regime dominates at high frequencies, and isothermal effects appear at low frequencies. The response of the microphone to a time varying pressure $p(t)$ is

$$\Delta p(t) = p(t) - h(t) * p(t) \tag{3}$$

where the impulse response of the low pass filter is represented by $h(t)$. The frequency response of the system is thus

$$\Delta p(\omega) = P(\omega) H(\omega) \tag{4}$$

where $H(\omega)$ is the frequency response of the low pass filter. The frequency response is a function of the acoustic resistance and capacitance via

$$H(\omega) = \frac{1}{1 + \imath \omega RC} \tag{5}$$

and the cutoff frequency of the filter is

$$f_{corner} = \frac{1}{2\pi RC}. \tag{6}$$

Since the sensor responds to pressure differentials between the backing volume and the atmosphere, this design results in sensitivity to high frequencies. Thus, low frequency variations such as weather disturbances are not detected, but higher frequency (infrasound and above) are captured. For further details and discussion, see Marcillo et al. (2012) and Appendix A of this report.

Values for the product of R and C (and thus f_{cutoff} and $H(\omega)$) can be determined by modeling the microphone's response to an instantaneous change in pressure p_0 via the following expression (Mutschlecner and Whitaker, 1997):

$$p(t) = p_0 e^{-\frac{t}{RC}}. \tag{7}$$

4 Microphone Calibration and Thermal/Vacuum Test Results

Each microphone was subjected to a series of pressure steps to determine the corner frequency of the mechanical filter. Pressure steps were created by detaching and then reattaching the mechanical filter to the transducer inlet. This increases the pressure in the backing volume above ambient pressure.

The corner frequency was determined by first deriving the product of acoustic resistance and capacitance by performing a linear least squares regression on the logarithm of the pressure decay with respect to time during each test (Equation 7). See Equation 6 for the corner frequency calculation. The regression domain was between A_{max} and $\frac{A_{max}}{e}$, where A_{max} was the maximum differential pressure or 100 Pa, whichever was lower. The corner period $\left(\frac{1}{f_{corner}}\right)$ for station TOP was 41 ± 16 seconds, station MID was 13 ± 2 seconds and station BOT was 39 ± 9 seconds. Equation 2 suggests that the corner period increases by several orders of magnitude in the stratosphere (see Figure 6 in Appendix A). Further details of microphone physics, corner period calculations, and effects of temperature and pressure on corner period are described in Appendix A.

The microphones and data acquisition system were tested in a thermal/vacuum chamber at the Columbia Scientific Balloon Facility in Palestine, Texas. The test consisted of the following:

1. Close chamber door, lower pressure to 1000 Pa, and backfill with dry nitrogen to 750000 Pa.

2. Cool chamber to -40 degrees Celsius.

3. Reduce pressure to 1000 Pa.

4. Backfill with dry nitrogen to 750000 Pa

5. Heat chamber to 40 degrees Celsius.

6. Reduce pressure to 1000 Pa.

7. Backfill with air and open chamber door.

The test took a total of 8 hours (Figure 8).

The mechanical low pass filters on station BOT and station TOP are similar, whereas the filter on station MID has a higher corner frequency. This is evident during the test, where MID recovers faster to pressure steps than BOT and TOP (Figure 9). Pressure values clip during pressurization and depressurization because the voltage produced by the microphones exceeds the data logger's dynamic range at high gain. The nominal range of linear response for the microphones is +/- 249 Pa (Marcillo et al., 2012), although the actual linear range is probably much higher. None of the microphones recovered to nominal pressure ranges during the initial pump down to stratospheric pressure. However, when the chamber was backfilled to 750000 Pa, the microphones generally remained within nominal range. When temperatures were low and pressure was reduced to 1000 Pa, station MID recovered to nominal range in a half hour and the other two stations took about 70 minutes. When temperatures were high and pressure was at 750000 Pa, the microphones remained at the high end of their linear range. This is because the test chamber increased in pressure, and thus had to be repeatedly purged, during the heating process (see pressure spikes around hour 6 in Figure 9). When temperatures were high and pressure was 1000 Pa, the microphones stayed well below nominal linear range. Station MID appears to re-equilibrate after a half hour, but the equilibrium line is at -1200 Pa. This indicates that a DC shift, perhaps due to a persistent pressure imbalance, exists at low pressures and high temperatures. Further testing will be necessary to determine if this is a common effect.

The presence of electromagnetic interference at 60 Hz may provide a calibration signal for the data acquisition system's frequency response to changing temperatures and pressures. We found that electromagnetic interference peaked at 60.0 Hz when the chamber door was open prior to the start of the test. The peak frequency during cooling at tropospheric pressure shifted upwards to 64.6 Hz, and rose to 66.9 Hz during cooling at stratospheric pressure. Station TOP was an exception; it dropped back to 60.0 Hz during cooling at stratospheric pressure. When the chamber was heated at tropospheric pressure, the electromagnetic interference peak frequency was 64.6 Hz. When the heated chamber was decompressed to stratospheric pressure, the peak frequency of BOT and MID increased to 64.9 Hz. Station TOP remained clipped during the final stratospheric depressurization. The highest pressures (when the chamber door was open) seem to correspond with the lowest peak frequencies, and the lowest pressures correspond with the highest peak frequencies. Temperature does not appear to affect the results. While this is intriguing, it is difficult to determine whether it is a consequence of innate pressure/frequency drift in the data acquisition system or a change in the thermal/vacuum chamber electronics AC frequency. An independent data logging system acquiring data at 150 Hz inside the thermal/vacuum chamber could distinguish between these effects, and perhaps should be present during future tests.

Pressure fluctuation power spectra are globally similar in different temperature and pressure conditions during the thermal/vacuum test (Figure 10). The lack of large fluctuations in the background acoustic spectra is encouraging; it does not give reason to suspect that changes in environmental conditions are affecting the frequency response of the microphones in the 0.01 to 100 Hz range. Several narrowband signals are apparent during the low pressure phases of the test. The signal source cannot be identified for certain, but the vacuum pump is a reasonable candidate. It must remain active during this portion of the test in order to maintain low pressure in the chamber. The vacuum pump is probably the cause of the sinc-like pulses during the warm ambient pressure part of the test as well. The pump turned on sporadically during this time because the increasing temperature also increased the pressure. The clipped pulses in Figure 9 correspond to times when the pump was observed to be active during the test. This clipping is probably responsible for the sinc-like shape of the pulses.

5   Scientific Results

The acoustic array recorded signals with frequencies spanning 5 orders of magnitude. The lowest frequency signals had periods of about 15 minutes and the highest at frequencies of 200 Hz (the Nyquist frequency of

the detector). The corner frequency of the microphone may distort the true pressure waveform for very long period signals. The higher frequency signals (> 40 Hz) are probably from sources proximal to the balloon, since attenuation increases with frequency.

The lowest frequency pressure signals recorded during flight have properties consistent with gravity waves. These phenomena consist of long period pressure fluctuations in which the restoring force is gravity. Typically, they are observed as periodic deviations in wind direction and temperature; the decrease in density with height leads to a large increase in amplitude in the middle atmosphere. Common sources of gravity waves include topography and convection, with wind shear and geostrophic adjustment contributing in less well understood ways. Gravity waves caused by mountains tend to be narrowband and stationary with respect to the Earth's surface, whereas convection-driven gravity waves are more broadband and propagate tens to hundreds of kilometers from the source. In general, gravity waves at a specific location and time tend to have narrow frequency spectra (Fritts and Alexander, 2003). Since the balloon passed over and nearby significant topography (Manzano Mountains and Mt. Taylor, both with a prominence of approximately 1500 m), the presence of orographic gravity waves is expected. Furthermore, thunderstorms and numerous cumulus clouds were observed on August 9, indicating that convectively driven gravity waves were also likely.

An example of gravity waves detected by station MID compared with elevation fluctuations is shown in Figure 11. A buoyant object oscillating in a pressure gradient will have elevation and pressure 180° out of phase, a phenomenon seen in the 20-30 minute time frame in Figure 11. However, pressure and elevation are typically in phase throughout the rest of the diagram, most notably between 0 and 15 minutes. The simplest explanation for this phenomenon is gravity wave perturbation causing the balloon envelope to rise and fall by several meters. Ensemble Hilbert spectrograms of long period pressure and altitude fluctuations show possible gravity wave signatures as well (Figure 12). Gravity wave energy shown here is concentrated in periods between 2000 and 500 seconds. While the elevation and pressure spectrograms agree at certain times (at 24000 seconds, for example), there appears to be significant differences as well (at 28000 seconds, for example). The high amplitude pressure fluctuations during ascent are absent from the elevation spectrogram, perhaps reflecting the presence of atmospheric turbulence or the effect of the balloon wake on the infrasound sensors.

The infrasound spectra recorded during the flight were generally similar across all three microphones, although station BOT had a relatively small low frequency response (Figure 13). Stations TOP and MID have a broad, low amplitude peak in the ocean microbarom frequency range (0.12 to 0.35 Hz; see Campus and Christie (2010)), whereas nearby ground stations do not. The ocean microbarom is a pervasive low frequency acoustic signal caused by wave interactions in the open ocean (Garcés et al., 2004). Its spectral signature is generally detected at night in calm conditions on the ground, when wind noise is at a minimum. The presence of this spectral peak on the airborne microphones and not on ground stations indicates that the flying stations may be comparatively more sensitive to low amplitude signals.

Prominent narrowband spectral peaks are present between 1 and 50 Hz. While their exact sources are difficult to identify without better horizontal coverage, they are most likely due to anthropogenic noise (aircraft, turbines, etc). A spectral peak at 1.8 Hz could be related to a wind power generation facility near Grants, New Mexico (Omar Marcillo, personal communication). A strong narrowband signal at 17 Hz is present on ground station ANMO and all three floating microphones as the balloon passes by (Figure 14). This demonstrates that infrasound is traveling from the surface to the stratosphere in this region.

The Fourier spectrogram of the ascent and float phases of the balloon reveals the full complexity of tropospheric and stratospheric infrasound (Figure 15). High amplitude broadband pressure fluctuations dominate the first half hour of flight as the balloon ascends through the troposphere. These fluctuations are likely a combination of wind noise (see Appendix B for a preliminary treatment of wind noise on a rising balloon) and turbulence from the balloon wake (Barat et al., 1984). Wind noise decreases in frequency and amplitude until it is negligible except at very low frequencies after an hour or so. The later stages of the ascent and the first part of float have numerous narrowband signals, some of which vary in frequency by several hertz. Stripes of broadband energy from 10000 seconds onward may correspond to air flow past the microphones due to either balloon motion or wind shear, but this is difficult to verify in the absence of anemometers. A few subtle downward-trending frequency bands in the 20-25 Hz may be the Doppler signature of aircraft; this is observed on the ground at station ANMO (10 km from the Albuquerque airport) as well. There is a general increase in broadband background noise as the day progresses.

Coherency is a measure of how two time series are related in the frequency domain (von Storch and

Zwiers, 1999). Coherent acoustic signals between microphones on the balloon indicate either acoustic waves or motion of the entire flight system through a density gradient. Conversely, incoherent signals imply pressure fluctuations with sources very near individual sensors (e.g. wind noise). Detection of coherent signals between airborne stations and ground stations provides strong evidence of a common acoustic signal. Coherency between stations TOP and BOT during the float portion of the flight is strong between 5 and 10 Hz and 15 and 20 Hz (Figure 16). However, the frequency and time resolution is poor, possibly excluding some of the more narrowband signals seen in the Fourier spectrogram (Figure 13). The bands of broadband pressure fluctuations are not evident on the coherency plot, indicating that they may be related to fluid flow past the sensor as opposed to acoustic waves.

A period of coherence at 17 Hz is visible between station TOP and the ANMO ground station as the balloon passes overhead (Figure 17). This coherence corresponds to the common spectral peaks observed on the two stations (Figure 14). Therefore, sensors on the ground and the stratosphere were recording the same acoustic signal for approximately one hour.

6   Anticipated Publications and Conference Abstracts

We will be submitting an abstract to the 2015 Seismological Society of America meeting in the special section "Observing Infrasonic Sources from Ground to Space." A letter-length manuscript will be prepared in Spring 2015 for submission to a peer-reviewed scientific journal. Results from this experiment will be included in Daniel Bowman's Ph. D. dissertation.

7   Team Demographics

The UNC 2014 HASP team consisted of the following:

Name	Gender	Race	Hispanic/Non Hispanic	Disabilities	Student Status	Institution
Daniel C. Bowman	Male	White	Non Hispanic	None	Graduate	UNC-CH
Patrick Gouge	Male	White	Non Hispanic	None	Undergraduate	UNC-CH
Tierney Larson	Female	White	Non Hispanic	None	Undergraduate	Yale University
Jacob F. Anderson	Male	White	Non Hispanic	None	Graduate	Boise State University

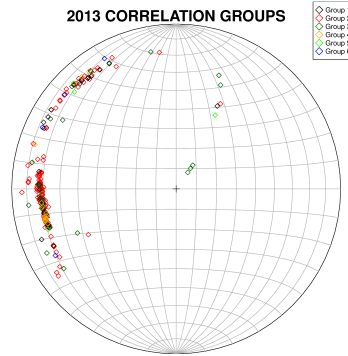Tierney Larson will be graduating this year.

8   Figures

Figure 1: Elevation-azimuth plot of acoustic arrivals at the SRG array south of of Albuquerque, NM. Arrivals at low incidence angle likely result from mine blasts and explosions from a New Mexico Tech facility. High incidence angle arrivals are of unknown origin.

Figure 2: Microphones enclosed in lunch coolers and attached to the flight ladder. This ladder runs between the gondola and the parachute during flight.

Figure 3: The acoustic array in the air several minutes after launch. Photo courtesy of T. Gregory Guzik.
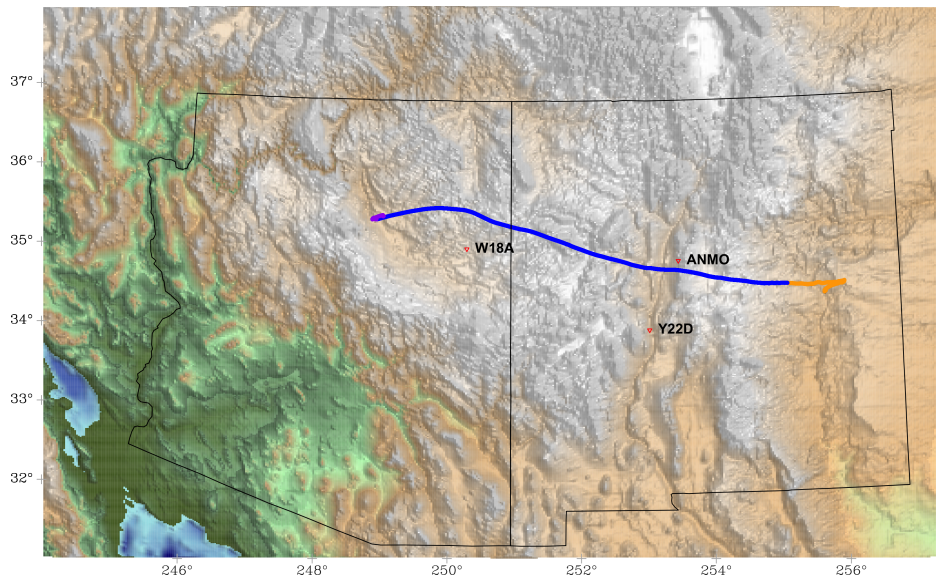
Figure 4: HASP flight path and ground infrasound stations used in this study. Orange is the ascent phase, blue is float phase, and purple is the descent phase of the flight.
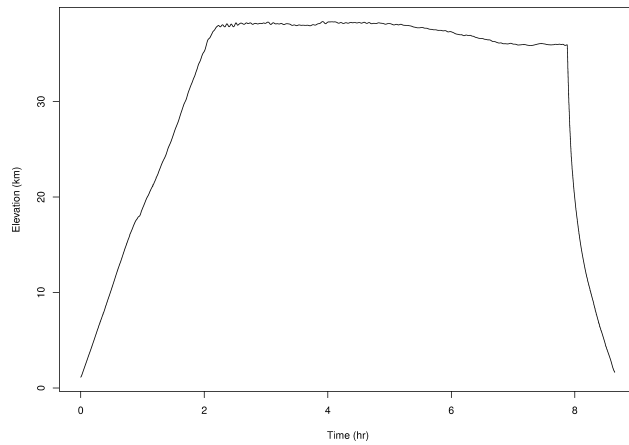
Figure 5: HASP flight elevation profile.
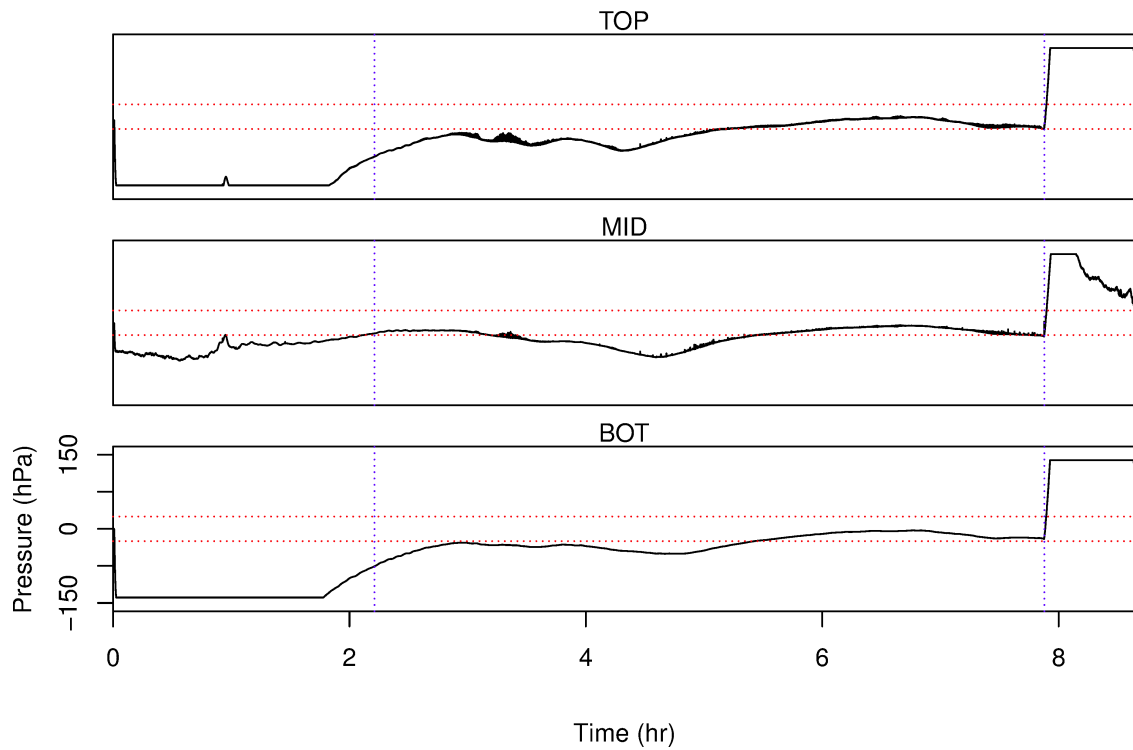
Figure 6: Pressure time series recorded on each microphone during flight. Horizontal dotted lines indicate the range of linear amplitude response. Vertical dotted lines indicate the ascent portion (left), float portion (middle), and descent portion (right) of the flight.
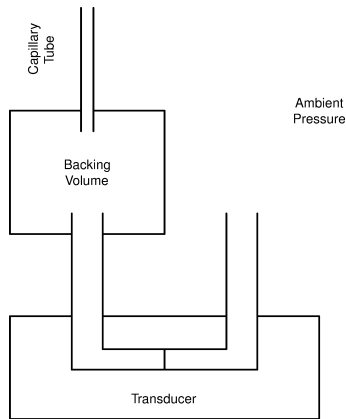
Figure 7: Schematic diagram of the InfraNMT mechanical high pass filter, modified after Figure 1b in Marcillo et al. (2012).
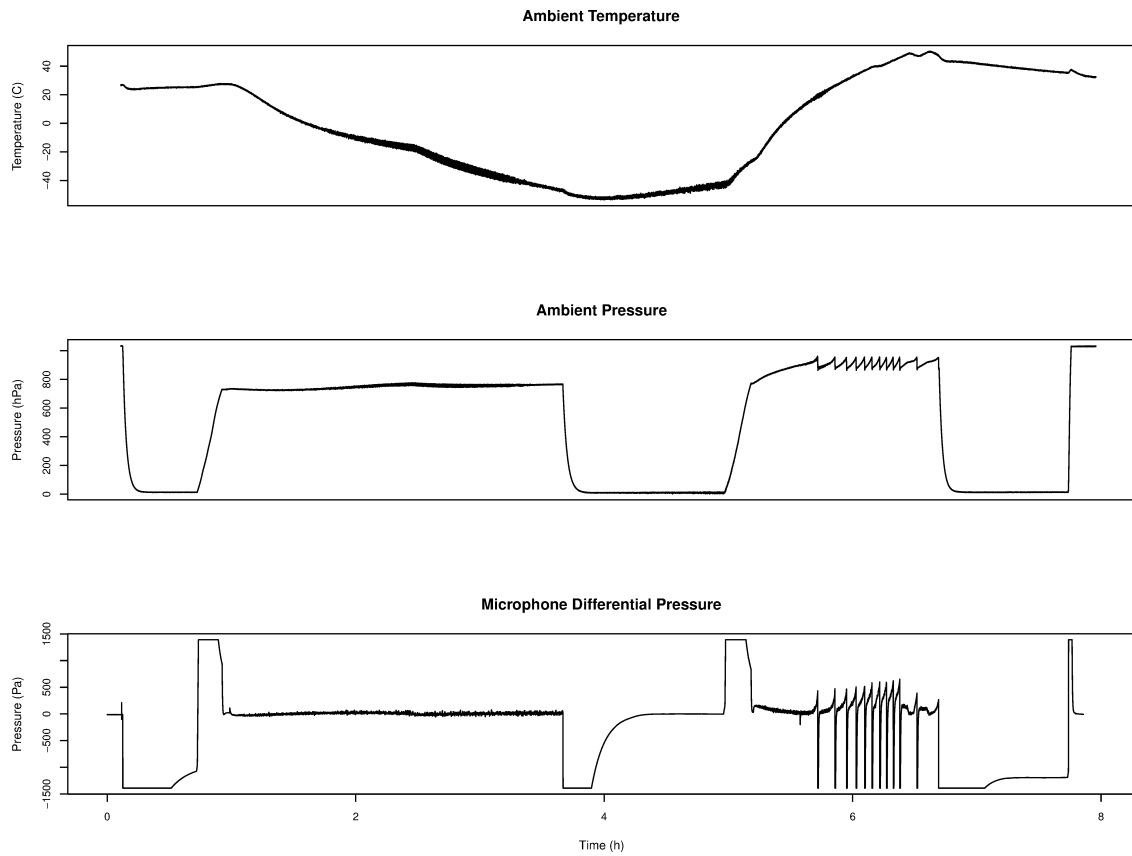
Figure 8: Temperature, ambient pressure, and infrasound microphone signals during thermal/vacuum test. Note the different y axis scales on ambient and differential pressure.
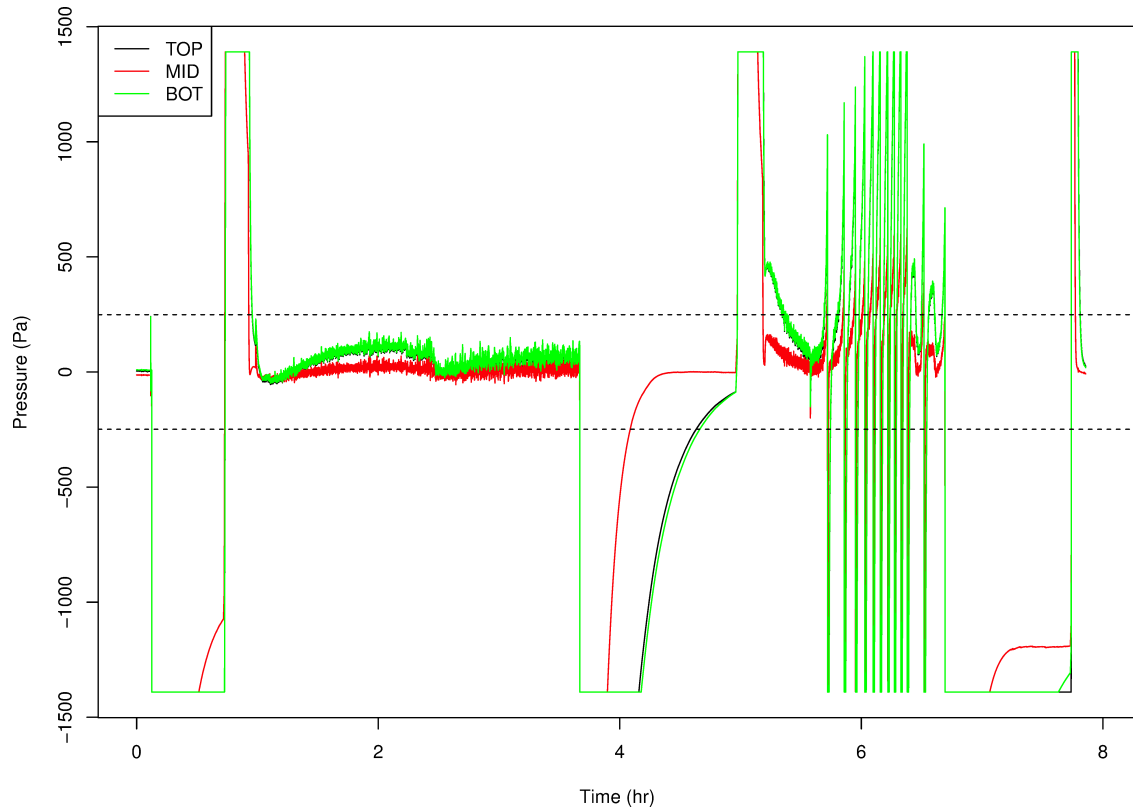
Figure 9: Pressure time series recorded on each microphone during the thermal/vacuum test. The dotted lines indicate the range of linear amplitude response.
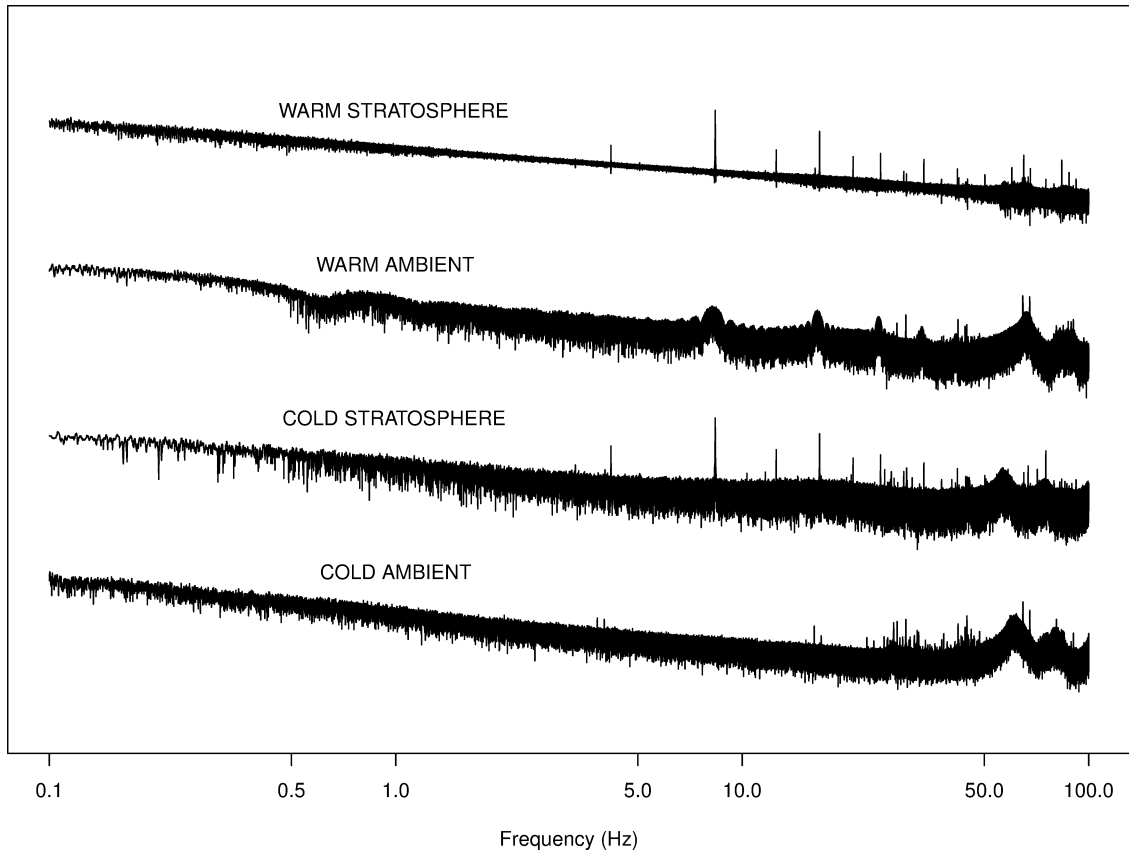
Figure 10: Scaled log power spectra of station MID during the thermal/vacuum test.
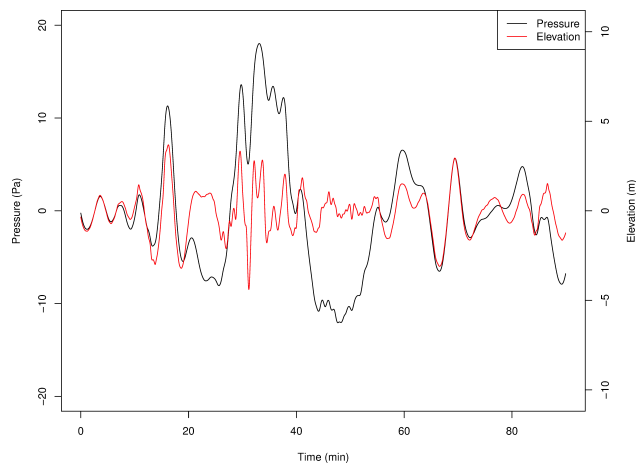
Figure 11: Ninety minutes of elevation and pressure fluctuations during float.
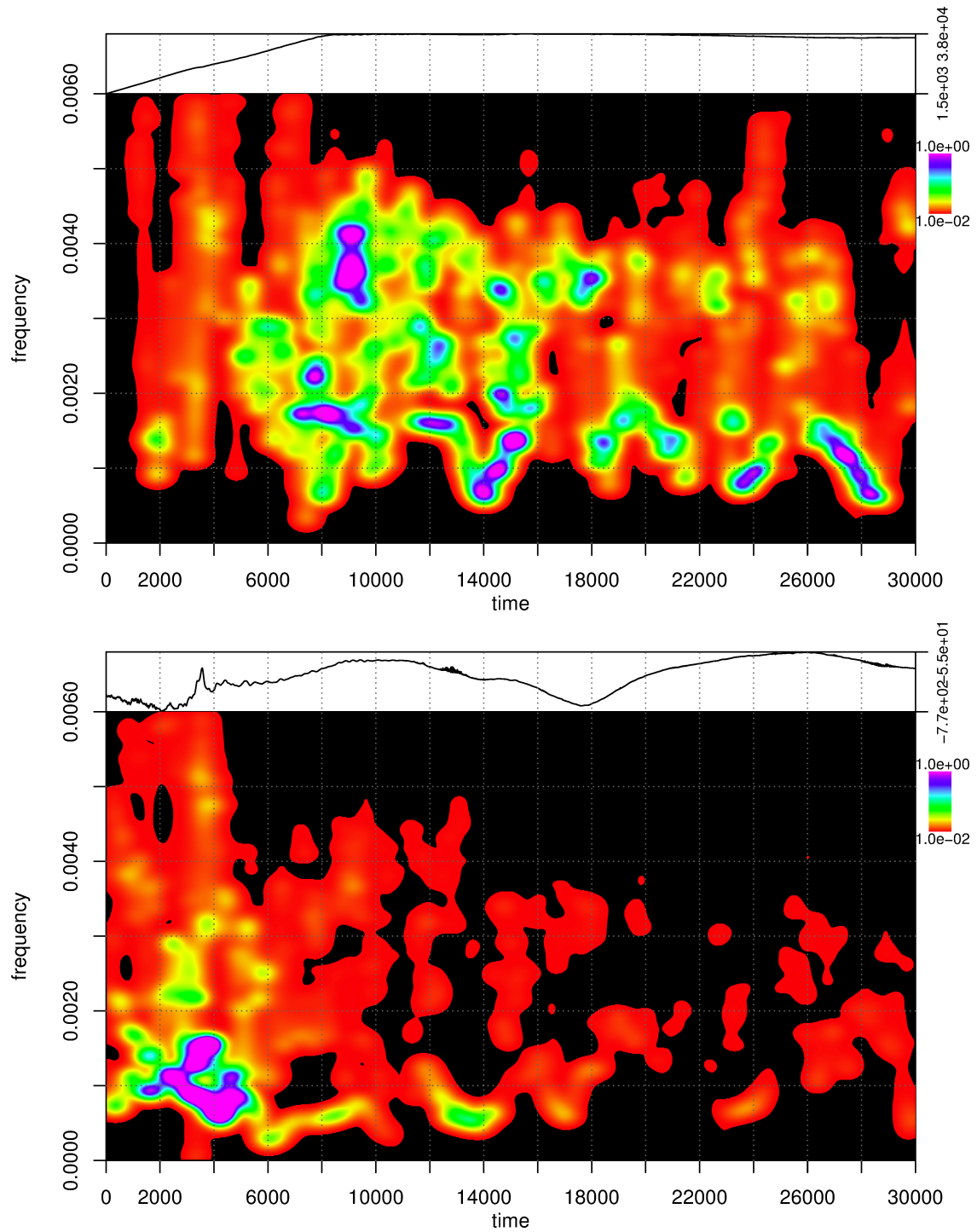
Figure 12: Ensemble Hilbert spectrograms of pressure on station MID (top) and gondola elevation (bottom) during ascent and float. Ascent takes place from 0 to approximately 8000 seconds.

13
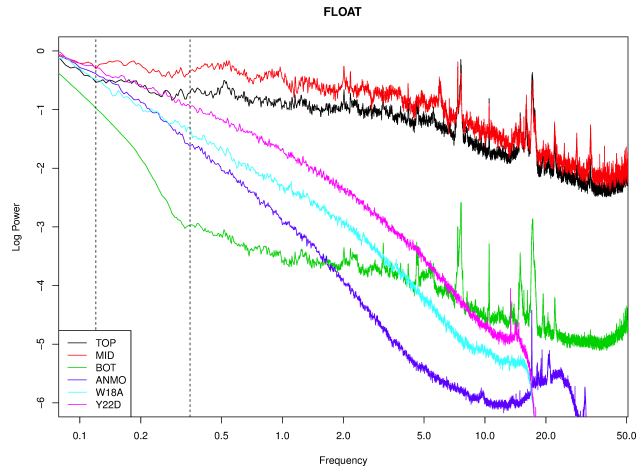
Figure 13: Normalized power spectra of HASP microphones compared with spectra of nearby ground infrasound stations. Dashed vertical lines indicate typical frequency range of the ocean microbarom. Nyquist frequencies are 50 Hz for station ANMO and 20 Hz for station Y18A and Y22D.
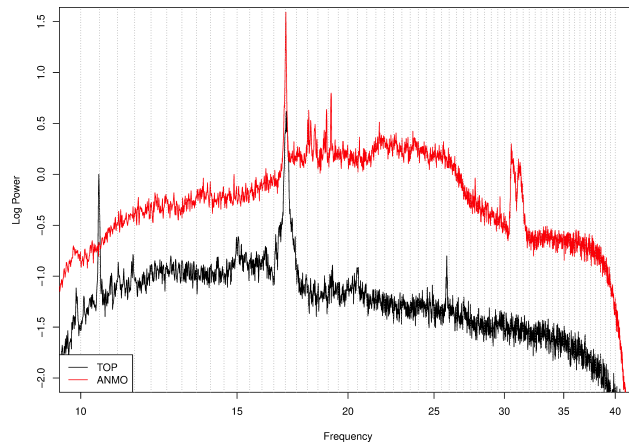
Figure 14: Normalized power spectra of station TOP compared with spectra of ground station ANMO during the hour in which the two stations were closest to each other. Data were bandpassed between 0.05 and 40 Hz.
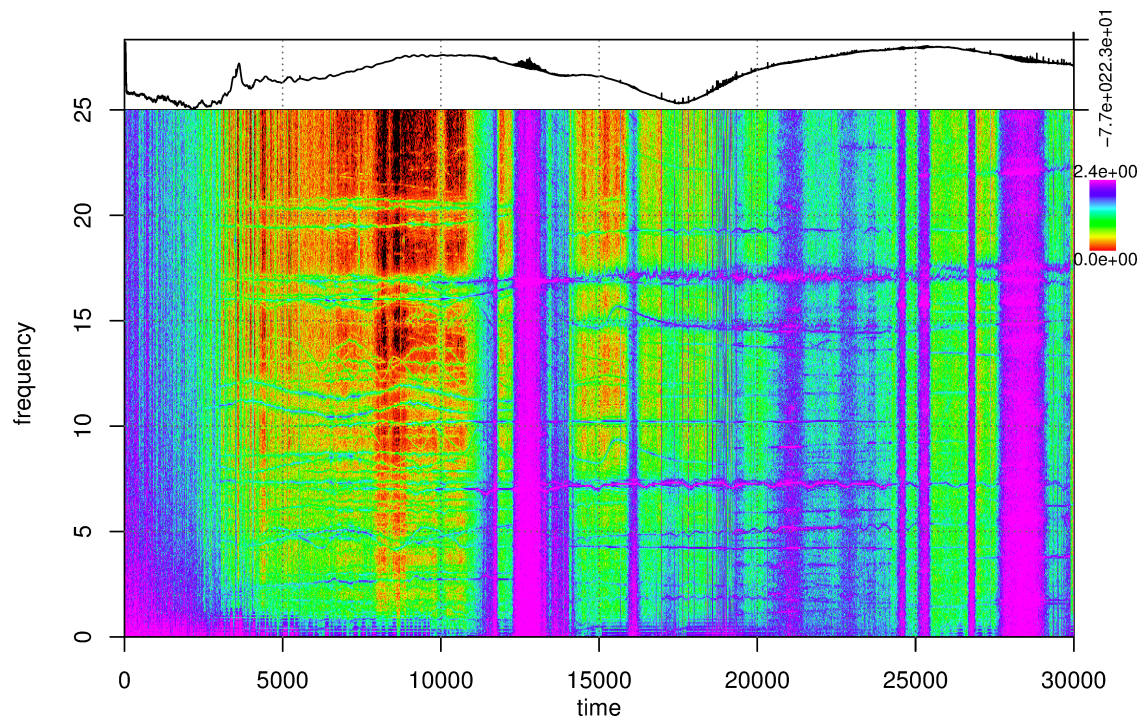
14

Figure 15: Fourier spectrogram of station MID during ascent and float. Ascent takes place from 0 to approximately 8000 seconds.
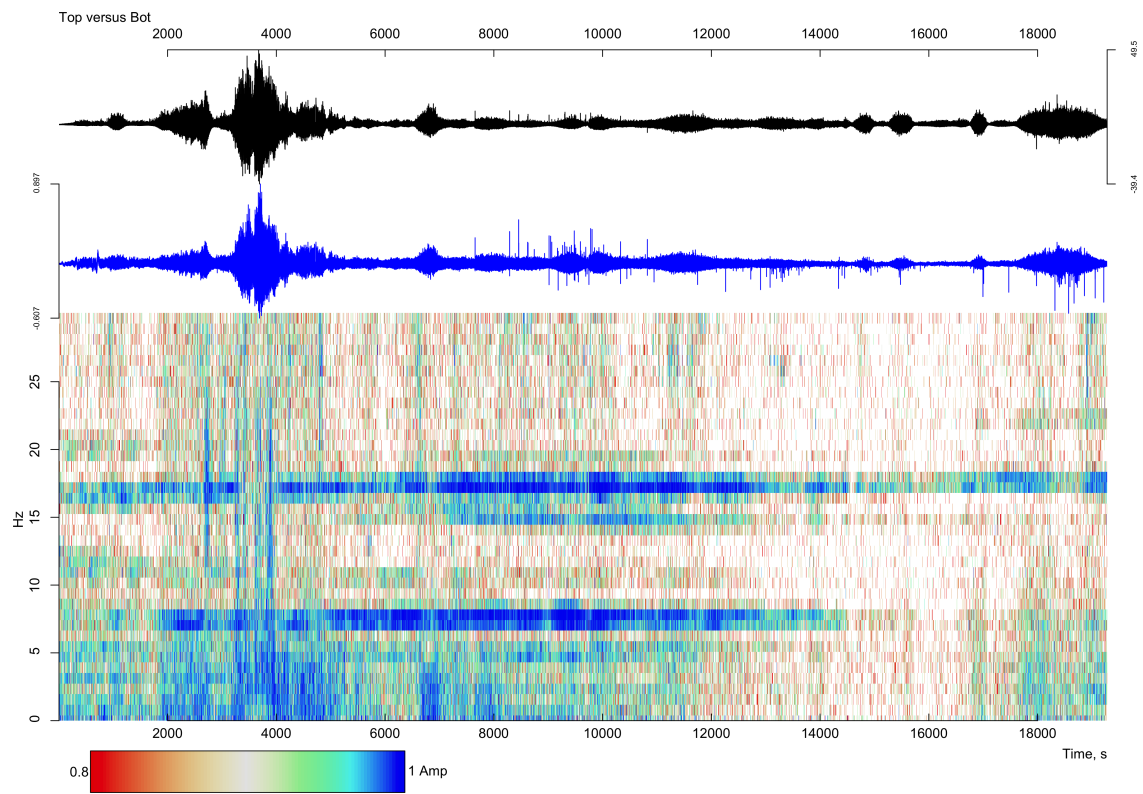
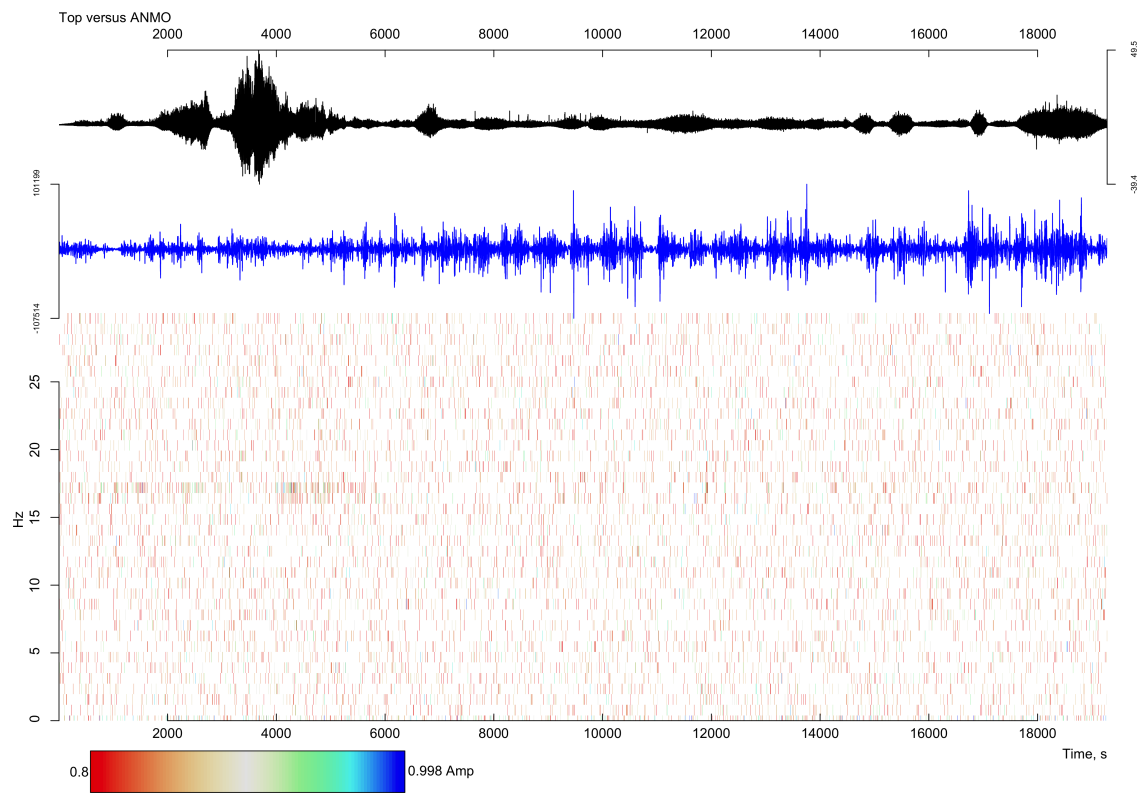Figure 16: Coherence between station TOP and station BOT during float.

Figure 17: Coherence between station TOP and station ANMO during float.

9 Acknowledgements

References

Barat, C., Cot, C., and Sidi, C. (1984). On the measurement of the turbulence dissipation rate from rising balloons. *Journal of Atmospheric and Oceanic Technology*, 1:270–275.

Bowman, D. C. and Lees, J. M. (2013). The Hilbert-Huang transform: A high resolution spectral method for nonlinear and nonstationary time series. *Seismological Research Letters*, 84(6):1074–1080.

Campus, P. and Christie, D. R. (2010). Worldwide observations of infrasonic waves. In Le Pichon, A., Blanc, E., and Hauchecorne, A., editors, *Infrasound Monitoring for Atmospheric Studies*, pages 185–234. Springer Science and Business Media.

Fritts, D. C. and Alexander, M. J. (2003). Gravity wave dynamics and effects in the middle atmosphere. *Reviews of Geophysics*, 41(1):1003.

Garcés, M. A., Willis, M., Hetzer, C., Le Pichon, A., and Drob, D. P. (2004). On using ocean swells for continuous infrasonic measurements of wind and temperature in the lower, middle, and upper atmosphere. *Geophysical Research Letters*, 31:L19304.

Marcillo, O., Johnson, J. B., and Hart, D. (2012). Implementation, characterization, and evaluation of an inexpensive low-power low-noise infrasound sensor based on a micromachined differential pressure transducer and a mechanical filter. *Journal of Atmospheric and Oceanic Technology*, 29:1275–1284.

Mutschlecner, J. P. and Whitaker, R. W. (1997). The design and operation of infrasonic microphones. Technical report, Los Alamos National Laboratories.

von Storch, H. and Zwiers, F. W. (1999). *Statistical analysis in climate research*. Cambridge University Press.

A Microphone Frequency Response Calculations

Determining the Frequency Response of a Differential Pressure Transducer

Daniel C. Bowman

December 8, 2014

1   Description of Instrument

A differential pressure transducer consists of two chambers separated by a diaphragm. One chamber has a port open to the environment, and the other has a port with a mechanical low pass filter attached. Pressure difference between the open chamber and the filtered chamber cause the diaphragm to deflect. Sensors on this diaphragm produce a voltage in response to the deflection (Figure 1). Additional details can be found in Marcillo et al. (2012) and Mutschlecner and Whitaker (1997).

The mechanical low pass filter consists of a backing volume connected to the environment via a capillary tube. The filter is conceptually equivalent to an electrical circuit consisting of a resistor and a capacitor in series. In this analogy, the capillary tube acts as a resistor and the backing volume is a capacitor. Pressure is equivalent to voltage and fluid flow through the capillary tube is equivalent to current. The result is a single pole low pass filter between the environment and one port of the transducer. Since the transducer only produces a signal when there is a pressure difference across the diaphragm, the end result is a high pass filter that is sensitive to transient fluctuations (i.e. infrasound) but does not detect broader pressure changes due to barometric or thermal forcing.

The acoustic resistance of the capillary tube is derived from the expression for Poiseuille flow (Mutschlecner and Whitaker, 1997):

$$R = \frac{8\eta}{\pi r^4} l \tag{1}$$

where η is the shear viscosity of the fluid, r is the radius of the capillary tube, and l is the length of the capillary tube. This expression assumes equilibrium laminar fluid flow in long cylinders.

The acoustic capacitance is

$$C = \frac{V}{\gamma \bar{P}} \tag{2}$$

where V is the backing volume, γ is the adiabatic gas constant, and $\bar{P}$ is the average background pressure. In Earth's atmosphere, the value of γ varies between 1.403 in pure adiabatic and 1 in pure isothermal conditions; this is dependent on the frequency of pressure fluctuations, air conditions, and chamber geometry (Marcillo et al., 2012). The adiabatic regime dominates at high frequencies, and isothermal effects appear at low frequencies.

The response of the microphone to a time varying pressure $p(t)$ is

$$\Delta p(t) = p(t) - h(t) * p(t) \tag{3}$$

where the impulse response of the low pass filter is represented by $h(t)$. The frequency response of the system is thus

$$\Delta p(\omega) = P(\omega)H(\omega) \tag{4}$$

where $H(\omega)$ is the frequency response of the low pass filter. The frequency response is a function of the acoustic resistance and capacitance via

$$H(\omega) = \frac{1}{1 + \imath \omega RC} \tag{5}$$

and the corner frequency of the filter is

$$f_{corner} = \frac{1}{RC}.$$

(6)

2 Calculating the Frequency Response

The expressions in the previous section depend on knowledge of RC, the product of acoustic resistance and acoustic capacitance in the mechanical filter. This product can be extracted by considering the time evolution a single pole low pass filter responding to a step function:

$$p(t) = p_0 e^{-\frac{t}{RC}}.$$

(7)

The expression above suggests two approaches. The first method involves measuring the time interval between an initial pressure p_0 and a final pressure $\frac{p_0}{e}$:

$$p_0 e^{-1} = p_0 e^{\frac{-t}{RC}}$$

Dividing through by p_0 and taking the logarithm gives

$$-1 = \frac{-t}{RC},$$

resulting in

$$t = RC.$$

Another, more statistically rigorous, approach involves taking the logarithm of both sides of Equation 7, yielding a linear expression with slope $\frac{-1}{RC}$:

$$\log p(t) = \log p_0 - \frac{1}{RC} t.$$

(8)

Performing a linear regression on this data provides an estimate and confidence intervals for RC. The quality of the model fit also allows a useful check on the performance of the mechanical filter with regards to its expected time evolution.

3 Testing Procedure

Pressure step functions can be generated by attaching a syringe to the mechanical filter and depressing the plunger slightly. Another simple method is to remove the mechanical filter from the transducer port and then reattach it. The second method tends to produce large overpressures. The result is a decaying exponential curve per Equation 7 (Figure 2). After flipping the time series around the x-axis and subtracting off the minimum value (if necessary), take the logarithm and fit a linear model using least squares regression (Figure 3). There is a small but systematic (nonrandom) misfit between the linear model and the data; this appears in most tests. This indicates that an RC-circuit model does not perfectly describe the behavior of these filters, and thus should be treated as a useful approximation rather than a comprehensive description.

An example test series is shown in Figure 4. These filters were attached to differential pressure transducers on board a high altitude balloon as part of the NASA HASP project. Stations BOT and TOP had the same type of filter, but station MID had a different capillary tube and a modified backing volume. BOT and TOP were tested 3 times each by recording the pressure decay when the filter was plugged into the transducer. MID was tested twice in this manner, and a further 3 times using a syringe. The similarities between BOT and TOP are apparent, but MID had a much lower corner period (approximately 10 seconds). In general, plug tests give more consistent results than syringe tests. This is evident on this plot as well as during tests not described here.

4 Environmental Effects on Corner Period

Differential pressure transducers should be tested in an environment similar to the one present during data acquisition. However, in some cases (such as stratospheric balloon flights), this may not be feasible. In these types of situations, changes to the RC term should be investigated to get a sense of the changes in frequency response that will occur. The two atmospheric parameters that affect RC are shear viscosity η and ambient pressure $\bar{P}$. An increase in η leads to an increase in R (see Equation 1) and thus an increase in corner period. Conversely, an increase in $\bar{P}$ leads to a decrease in C (see Equation 2) and thus a decrease in corner period.

Shear viscosity is nearly independent of pressure, but it does vary with temperature. Sutherland's formula

$$\eta = \eta_0 \frac{T_0 + 110.3}{T + 110.3} \left(\frac{T}{T_0} \right) \tag{9}$$

where η_0 is a reference viscosity at temperature T_0 (in Kelvin), describes the shear viscosity of air between about 100 and 1900 Kelvin (Ames Research Staff, 1953). The expected variation in corner period due to temperature alone is shown in Figure 5. Since pressure decreases by two orders of magnitude between the surface and the stratosphere, it will have a greater effect on the corner period than temperature. A plot of corner period versus altitude for a typical day in Chapel Hill is shown in Figure 6. The extreme increase in corner period in the stratosphere implies that microphones on high altitude balloon flights should have small backing volumes.

References

Ames Research Staff (1953). Equations, tables, and charts for compressible flow. Technical report, National Advisory Committee for Aeronautics. Report 1135.

Marcillo, O., Johnson, J. B., and Hart, D. (2012). Implementation, characterization, and evaluation of an inexpensive low-power low-noise infrasound sensor based on a micromachined differential pressure transducer and a mechanical filter. *Journal of Atmospheric and Oceanic Technology*, 29:1275–1284.

Mutschlecner, J. P. and Whitaker, R. W. (1997). The design and operation of infrasonic microphones. Technical report, Los Alamos National Laboratories.
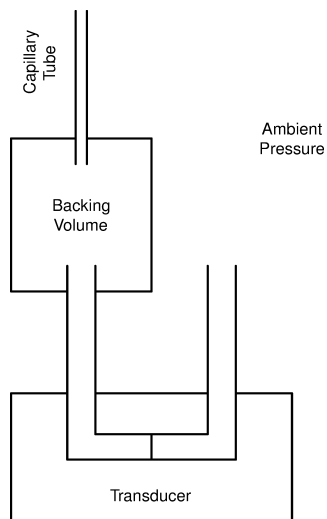
5 Figures

Figure 1: Schematic diagram of InfraNMT mechanical high pass filter, modified after Figure 1b in Marcillo et al. (2012)
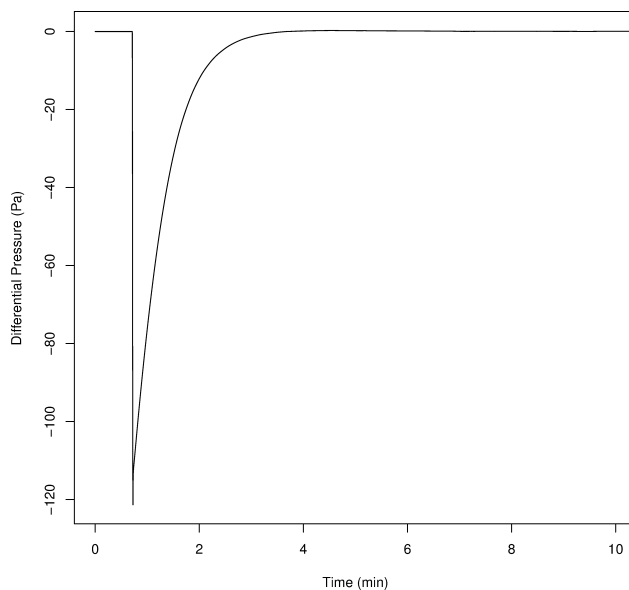

Figure 2: Response of differential pressure transducer when the mechanical filter is unplugged, then plugged back in. This pressurizes the backing volume, resulting in a negative differential pressure.
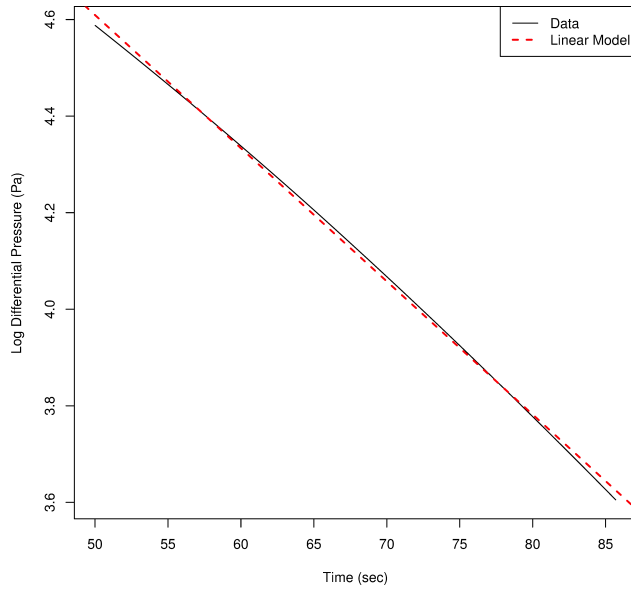
Figure 3: A linear least squares regression model applied to time versus the logarithm of pressure. The slope of the regression line is related to the product of acoustic resistance and acoustic capacitance per Equation 8.
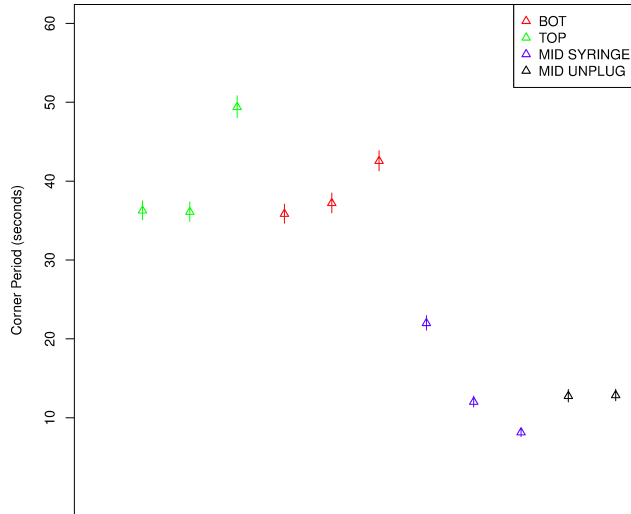

Figure 4: Example of test data from the 2014 NASA HASP project. Filters BOT and TOP were the same model, but filter MID had a different backing volume and capillary tube. BOT and TOP were both tested by unplugging and plugging in the filters, MID SYRINGE was tested using a syringe to pressurize the filter. The lines represent 95% confidence intervals.
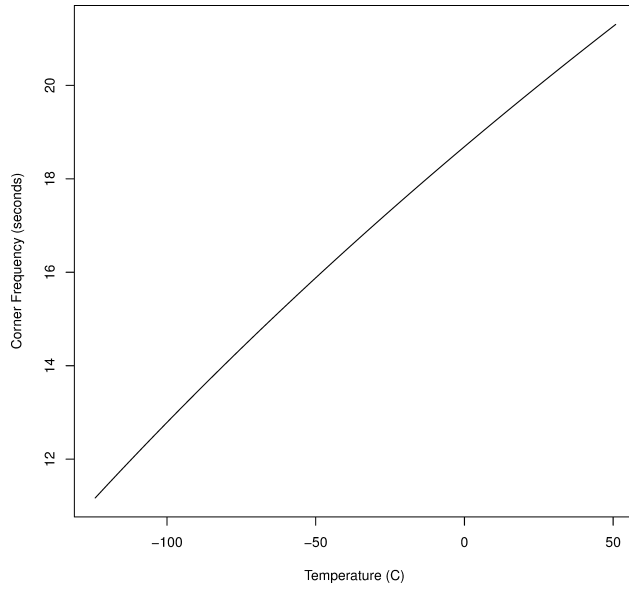
Figure 5: Corner frequency variation with temperature.
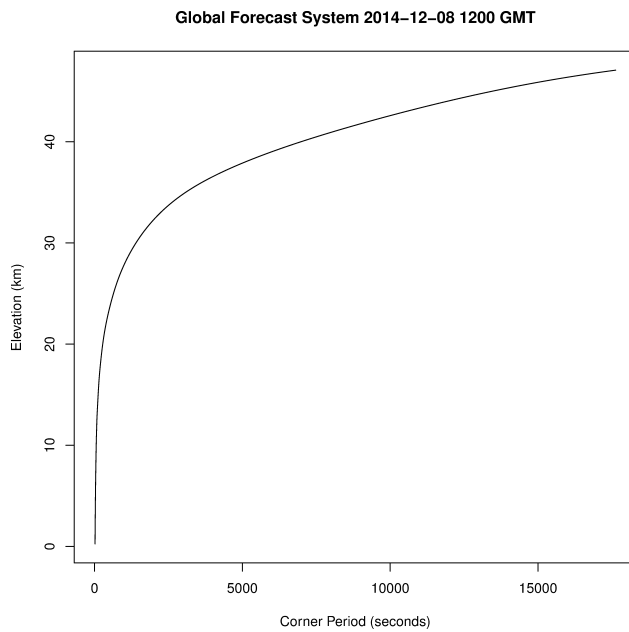
Global Forecast System 2014–12–08 1200 GMT

Figure 6: Corner period with height over Chapel Hill, North Carolina. The filter has a corner period of 20 seconds at 25 Celsius and 1000 millibars.

B   Wind Noise on a Free Flying Microphone

Wind Noise on a Free Flying Microphone

Daniel C. Bowman

April 16, 2014

1   Introduction

Wind-related noise is a pervasive element of outdoor acoustic recordings. While several studies have explored wind noise and its mitigation on microphones located near the Earth's surface (e. g. Walker and Hedlin (2010); Hessler et al. (2008); Raspet et al. (2006)), there is a lack of information on how it varies in the free atmosphere. This study investigates the properties of wind noise in the troposphere and lower stratosphere recorded by a video camera on board a large hydrogen-filled balloon. Wind noise as a result of fluctuating stagnation pressure is modeled, and other wind noise sources such as atmospheric turbulence and Helmholtz resonance are discussed. Results from this experiment will inform sensor design for the upcoming launch of an infrasound array on board a NASA high altitude balloon.

2   Wind Noise Theory

Wind noise is a significant problem for infrasound networks worldwide. This signal is a result of three processes: sensor-wind interaction, pressure variations advected across the sensor, and sound generated by the wind itself (Walker and Hedlin, 2010). The interaction of the sensor with the wind produces a pressure signal with a power spectrum that scales as the wind velocity squared and the fluid density squared:

$$P_s(k) = \rho^2 \bar{u}^2 |\overline{V(k)}| \tag{1}$$

where $\bar{u}$ is average wind velocity and $V(k_1)$ is the power spectral density of the wind velocity for wavenumber k. Coherent pressure fluctuations carried across the sensor by the wind also contribute to noise levels. These fluctuations are typically the result of turbules advected across the sensor. The frequency of this type of wind noise depends on the length scale of the turbules and the wind velocity. Finally, wind can interact with objects on the surface of the Earth to create acoustic energy, which is then recorded on the microphone (Walker and Hedlin, 2010).

Helmholtz resonance is a fourth possibility for sensors contained in chambers exposed to the wind. Pressure fluctuations due to vortex shedding or ambient turbulence can excite the resonant frequencies of the cavity. This frequency is controlled by the fluid and cavity as outlined by

$$f_H = \frac{c}{2\pi} \sqrt{\frac{A}{V d_{eff}}} a \tag{2}$$

where c is the speed of sound, A is the area of the cavity opening, d_{eff} is the effective acoustic wave length as a function of neck length of the cavity, and V is the volume of the cavity. This phenomenon is equivalent to the "side window buffeting" experienced in passenger cars moving at highway speeds (Singh et al., 2010).

3   Experiment

A Kodak PlaySport video camera and an Arduino-based high altitude GPS chip were lifted into the stratosphere using a 600 gram mylar balloon filled with hydrogen gas. The balloon was launched near Saxapahaw, North Carolina, and the payload landed near Selma, North Carolina; the maximum altitude achieved was

24 kilometers (Figure 1). The horizontal velocity of the payload ranged from near zero at launch to about 160 km/hr at the top of the troposphere. The balloon recorded a 65 km/hr horizontal wind just before it burst. The balloon ascended at about 8 m/s just after launch, reaching around 10 m/s just before burst. The payload descended at about 65 m/s at the beginning of its fall, and struck the ground at approximately 15 m/s.

4   Acoustic Signals Recorded During Flight

The video camera detected discrete events during the balloon flight as well as continuous acoustic signals attributed to wind noise. Discrete events include the periodic clicking of the camera shutter, the weather balloon burst at the top of the trajectory, and the payload striking the ground at the end of the flight (Figure 2). The amplitude of the continuous wind signal decreased during the ascent, but remained approximately steady during the descent (Figure 3).

The root mean square (RMS) amplitude over successive 15 second windows was computed to quantify the variation of average acoustic amplitude throughout the flight. The RMS amplitude drops by a factor of three during the ascent from the Earth's surface to 24 km (Figure 4). The sound level during the descent was slightly higher than the maximum sound level during the ascent. However, the RMS amplitude plot does show an abrupt decrease in sound level over the last two thirds of the descent; this is not apparent in the raw time series.

The Fourier spectrogram of the acoustic signal reveals several frequency patterns during the ascent (Figure 5). A low amplitude, high frequency (150-250 Hz) signal was recorded for about the first ten minutes of flight. A second signal glides from about 50 Hz to almost 150 Hz during the first 1500 seconds of ascent. Most energy is focused below 50 Hz, with energy decreasing significantly after about 2500 seconds. Sound levels during the descent are concentrated below 100 Hz, with most energy below 50 Hz.

5   Determining Payload Velocity and Atmospheric Density

Wind noise depends on air density, wind velocity, and sound velocity as outlined above. Thus, an empirical model can be constructed that relates these factors to the magnitude of the acoustic signal recorded by the video camera. In order to do this, the payload's ascent and descent rate must be determined from GPS tracker data, whereas atmospheric density must be estimated from operational weather prediction models.

The height h of the balloon at time t is a travel time problem:

$$t_n = \sum_{i=0}^{n} l_n v_n \tag{3}$$

where the time t_n elapsed when the balloon reaches a certain elevation depends on the thicknesses l_n and vertical velocities v_n of all the layers below it. The bursting of the balloon represents a discontinuity, so the ascent velocities and descent velocities are calculated separately.

The ascent and descent velocity was derived using a first order Tikhonov regularization scheme to ensure a smooth model (Figure 6). The regularization parameter for the ascent velocity was chosen using the L-curve minimization method. The descent velocity did not show a clear L curve so a regularization parameter was chosen by inspection. Poor GPS performance between 13 and 18 kilometers above sea level complicated the ascent velocity calculations. Therefore, elevation data from this interval were rejected, and that portion of the atmosphere was considered as a single layer.

Atmospheric density was determined using archived Near Real Time Global Forecast System results (3 hour prediction generated by the March 30th, 2013 1200 GMT model run). An atmospheric profile was generated at the midpoint of the balloon flight and density was calculated via

$$\rho = \frac{p}{R_s T} \tag{4}$$

where ρ is density, p is pressure in pascals, R_s is the specific gas constant for dry air, and T is temperature in Kelvin. Atmospheric density varies by an order of magnitude over the flight ((Figure 6).

6 Wind Noise Modeling

The relationship expressed in Equation 1 suggests that noise levels should be proportional to fluid density multiplied by velocity if the signal generation mechanism is related to fluctuations in stagnation pressure. Thus a linear model should appropriately explain the relationship between sound level and the product of fluid density and velocity (Figure 7). A chi-square goodness of fit test indicates that there is no reason to suspect the residuals of each model are not normally distributed at a 95% confidence level. During the ascent, the model indicates that sound level decreases as the payload velocity increases and atmospheric density decreases. However, the sound level increases as the velocity multiplied by density decreases when the payload is descending.

7 Discussion

The continuous acoustic signal recorded on the video camera could have resulted from three sources: fluctuations in stagnation pressure, advection of turbulence across the sensor, and Helmholtz resonance of the cavity in which the microphone was placed. The latter two possibilities will produce an acoustic signal that changes in frequency as the velocity of the camera and the density of the atmosphere vary though the flight. In particular, a Helmholtz resonator should drop in frequency with decreasing sound speed (Equation 2). There is an apparent increase in frequency during the first 2000 seconds of the flight (Figure 5), which does not match the expected behavior of a Helmholtz resonance signal. This is because the temperature, and thus the sound speed, decreases in the troposphere. The increase in ascent rate and changes in turbulence length scale in the atmosphere could potentially explain the observed frequency gliding. However, the lack of knowledge about the length scales of atmospheric turbulence at different elevations as well as how the frequency response of the camera depends on temperature make it difficult to draw definitive conclusions about the cause of the frequency gliding.

The linear relationship between acoustic amplitude and the product of density and velocity during the ascent phase of the flight agrees well with the model of stagnation pressure fluctuations outlined in Equation 1. Furthermore, the sound level did not appear to vary with horizontal wind speed. Thus, wind conditions in the atmosphere have a relatively small effect on the acoustics of a free-flying balloon, whereas atmospheric density and the balloon's ascent rate exerts a much stronger control. The apparent decrease in acoustic amplitude with the product of density and velocity during the descent is puzzling. In contrast to an ascending balloon, the velocity of a payload at terminal speed is related to the square root of density. This relationship could be affecting both the decrease in amplitude as well as the much narrower amplitude range observed as the payload fell back to Earth.

References

Hessler, G. F., Hessler, D. M., Brandstätt, P., and Bay, K. (2008). Experimental study to determine wind-induced noise and windscreen attenuation effects on microphone response for environmental wind turbine and other applications. *Noise Control Engineering*, 56(4):300–310.

Raspet, R., Webster, J., and Dillion, K. (2006). Framework for wind noise studies. *Journal of the Acoustical Society of America*, 119:834–843.

Singh, A., Rajvanshi, D., and Nikam, K. (2010). Buffeting noise computations for an open side window. In *Proceedings of the 37th National and 4th International Conference on Fluid Mechanics and Fluid Power*, Madras, Chennai, India.

Walker, K. T. and Hedlin, M. A. (2010). A review of wind-noise reduction technologies. In *Infrasound Monitoring for Atmospheric Studies*, chapter 5, pages 141–182. Springer Science and Business Media.
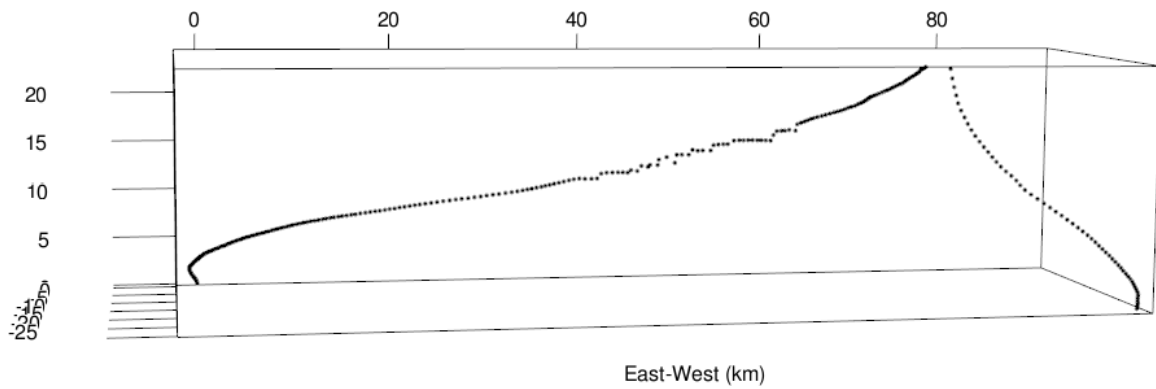
8 Figures

Figure 1: Flight path of weather balloon with microphone over central North Carolina. Axes are distances in kilometers from the launch site.
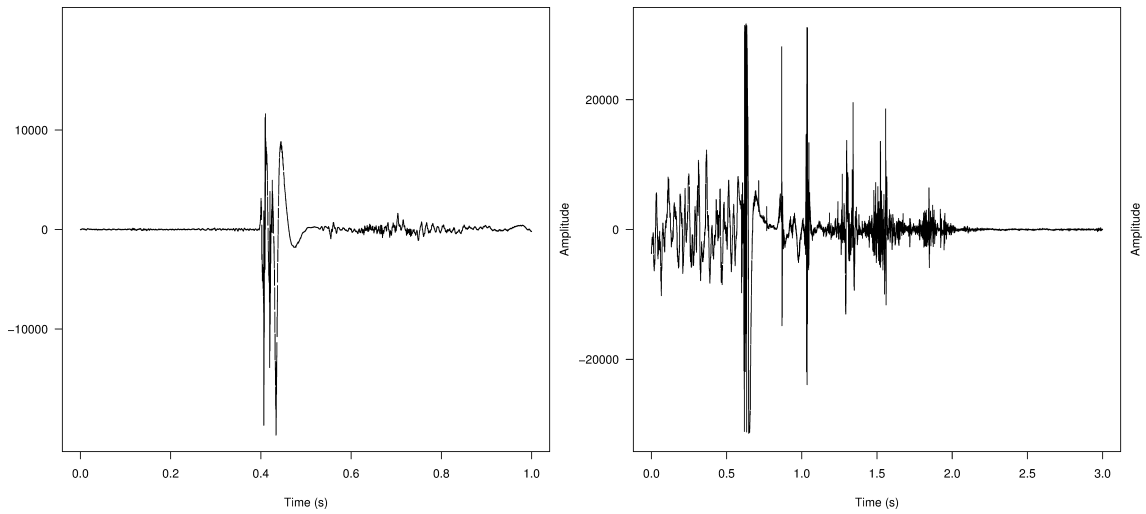
Figure 2: Balloon burst (left) and payload impact (right) recorded on video camera microphone. Amplitude is in arbitrary units.
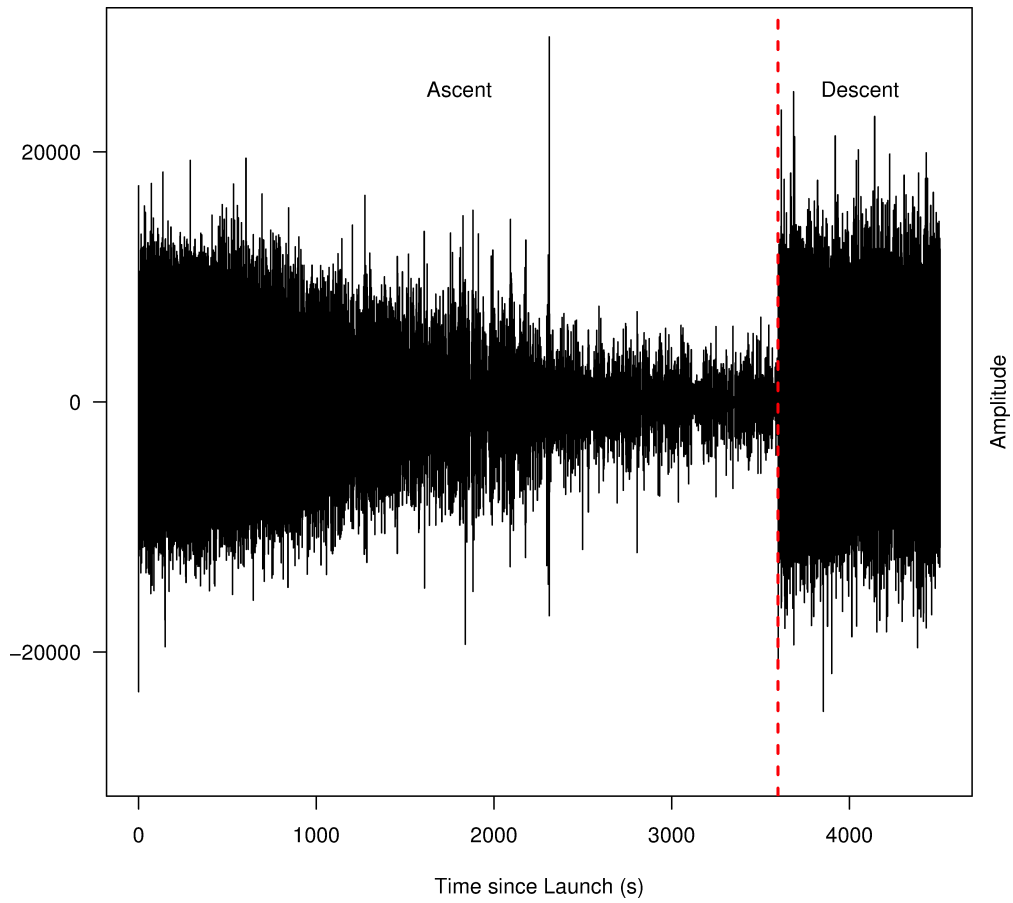

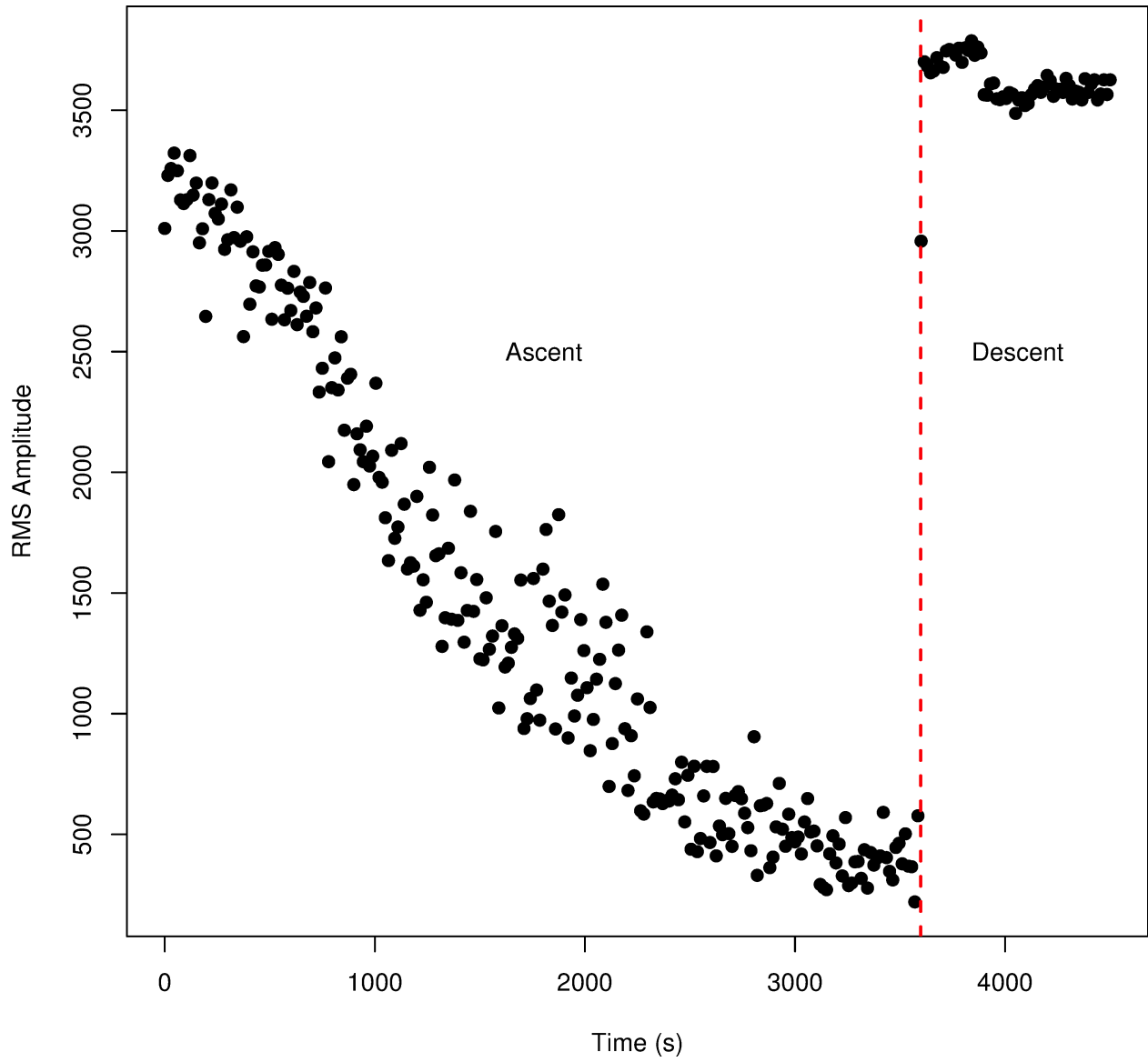Figure 3: The acoustic signal recorded during the balloon flight.

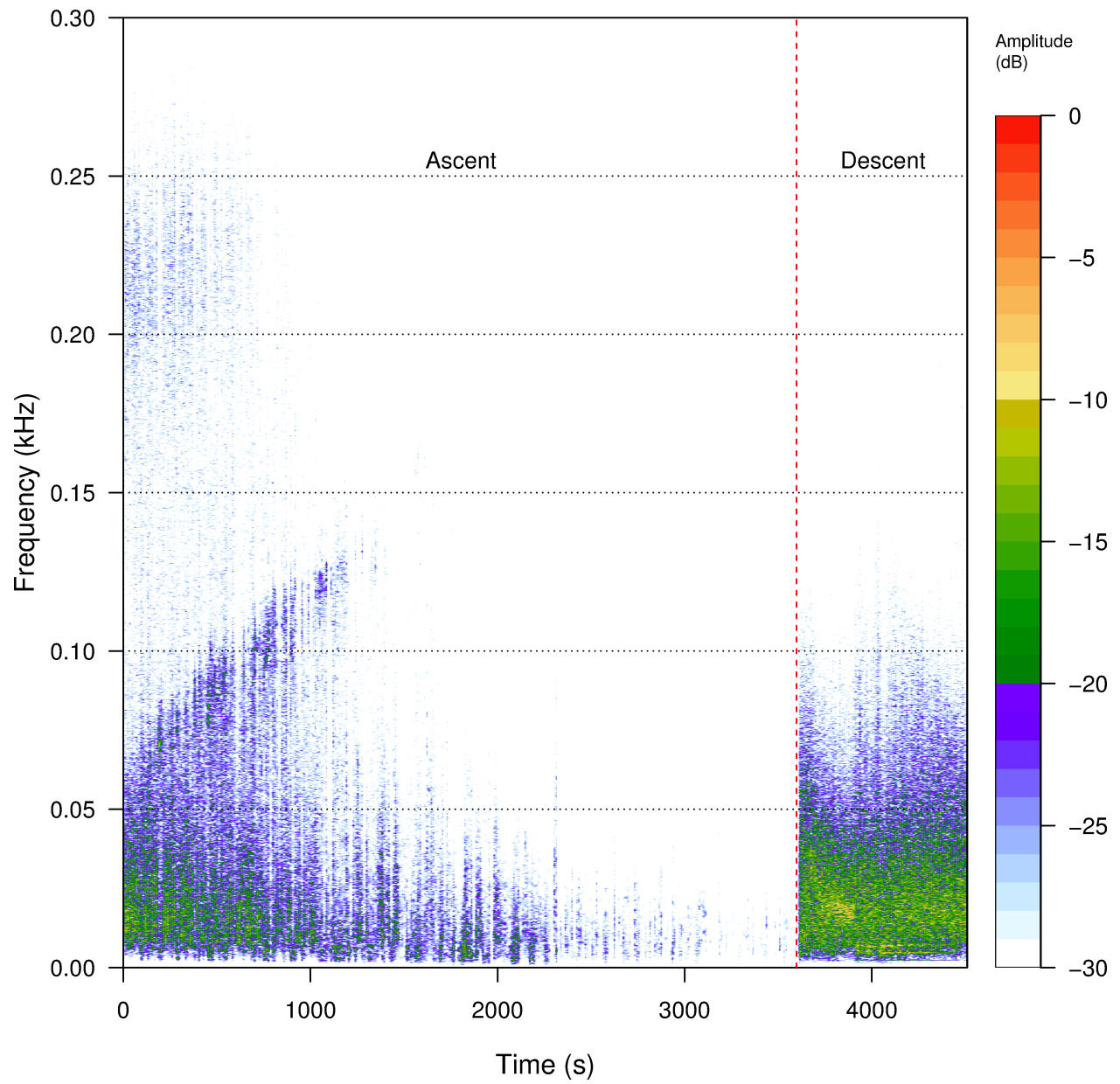Figure 4: Root mean square amplitude averaged over a 15 second window.

Figure 5: Fourier spectrogram of acoustic signals recorded during the balloon flight.
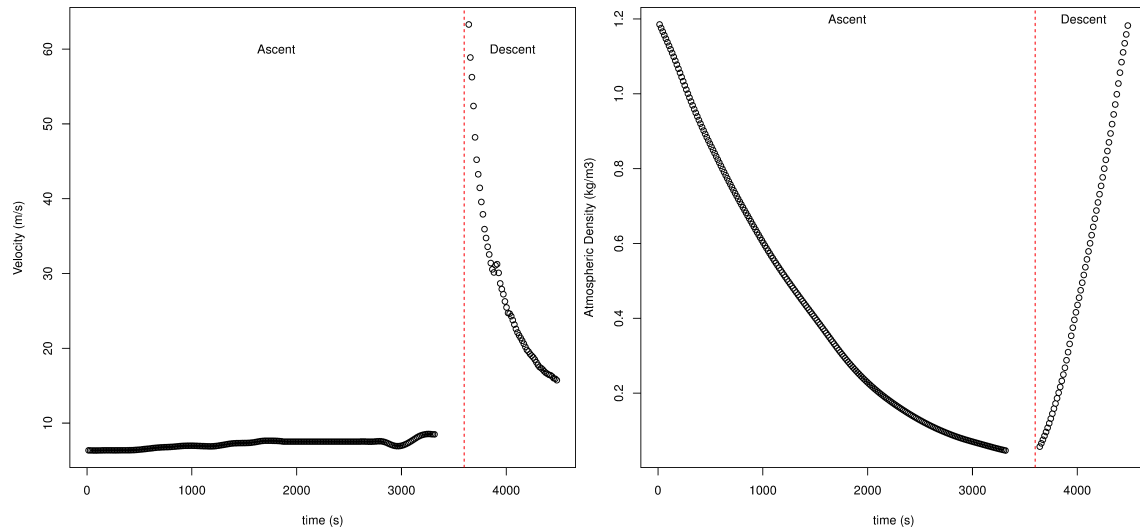
Figure 6: Balloon velocity model derived using 1st order Tikhonov regularization (left) and density model derived from operational weather forecast data (right). Data gap before balloon burst is due to loss of GPS fix.
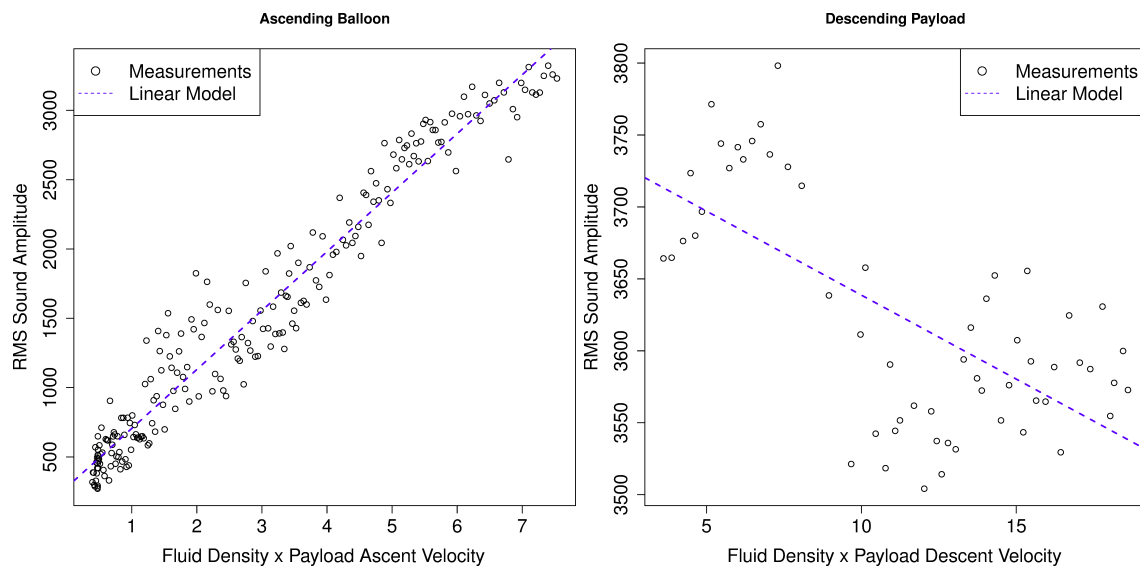

Figure 7: Linear models of sound level versus atmospheric density and payload velocity.